Simulation of Vortex Core Precession in a Reverse-Flow Cyclone

J. J. Derksen and H. E. A. Van den Akker
Kramers Laboratorium voor Fysische Technologie, Delft University of Technology, Prins Bernhardlaan 6, 2628 BW Delft, The Netherlands

A large-eddy simulation of the single-phase turbulent flow in a model cyclone geometry on a uniform, cubic computational grid consisting of 4.9×10^6 cells was performed. The Navier-Stokes equations were discretized according to a lattice-Boltzmann scheme. The Reynolds number, based on the inlet velocity and the cyclone body diameter, was 14,000. A standard Smagorinsky subgrid-scale model with $c_s = 0.1$, including wall-damping functions, was applied. The 3-D, average flow field was predicted with a high level of accuracy. Furthermore, the simulations exhibit vortex-core precession, that is, the core of the main vortex is observed to move about the geometrical axis of the cyclone in a quasi-periodic manner. The Strouhal number associated with the simulated vortex-core precession was 0.53, whereas 0.49 was experimentally observed in a similar geometry at approximately the same Reynolds number.

Introduction

Flow prediction in cyclones

As in many confined swirling flow systems, the hydrodynamic phenomena in cyclones can be of a complex nature. Flow reversal, (quasi-) periodic fluctuations, and strongly anisotropic turbulence are some of the characteristics. A prominent industrial application of swirling flow is found in cyclone separators that are, for example, used for cleaning gas streams from dust particles or for catalyst recovery. By introducing the particle-laden gas tangentially into the reverse-flow cyclone, a strong vortex is created that will centrifuge the particles toward the wall. The gas is forced to flow downwards to the base of the cyclone in a spiraling motion. At the base, the particles can be collected, whereas the cleaned gas moves upwards toward the exit pipe. Simulation of the flow field in a cyclone bares the promise of being able to predict the pressure drop and the separation efficiency as a function of the particle size. In high-efficiency cyclones that are used to recover the smallest particles (down to 2 μm) in the final stages of a separation process, the solids loading is sufficiently low to allow for simulations based on a one-way coupling between the gas-phase flow field, and the particulate flow. In more highly loaded systems, two-way coupling (that is, the effect the particles have on the gas-phase flow), and particle–particle collisions need to be taken into account. In any case, an accurate simulation of the (single-phase) gas flow is prerequisite for meaningful cyclone modeling.

The complexity of the flow field, however, makes accurate predictions a difficult task. Many articles dealing with predictions on the single-phase flow in cyclones treat the flow field as being axisymmetric (such as Boysan et al., 1982; Zhou and Soo, 1990; Dyakowski and Williams, 1993) and steady. The reason for this is obvious: three-dimensional simulations in a complexly shaped flow domain are computationally very demanding, especially when using the advanced turbulence models that are necessary to capture the anisotropy of the turbulence induced by swirl (Hoekstra et al., 1999). There are, however, some intriguing issues that motivate a 3-D, and time resolved simulation. In the first place, with a three-dimensional simulation the assumptions made in an axisymmetric simulation, for example, with respect to the inlet boundary conditions, can be assessed. In the second place, cyclones exhibit a highly nonaxisymmetric, low-frequency instability, known as the precessing vortex core (PVC) (Gupta et al., 1984; Yazdabadi et al., 1994; Griffiths, et al. 1998). The PVC is a quasi-periodic motion of the core of the main vortex about the cyclone's geometrical center. Experimental studies of

Correspondence concerning this article should be addressed to J. J. Derksen.

swirling flow reveal the strong impact of vortex core precession on the level of the velocity fluctuations (Wunenburger et al., 1999). Near the center, typically 80% of the kinetic energy of the fluctuations is contained in coherent fluctuations near the center of a cyclone, which might be attributed to the PVC (Hoekstra et al., 1998a). We therefore suspect that the PVC strongly influences the flow phenomena in cyclones. Furthermore, according to Griffiths et al. (1998) the quasi-periodic fluctuations induced by the PVC might lead to large-amplitude pressure fluctuations, and hence mechanical failure. In the third place, the solid particles that need to be separated from the gas stream do not feel the average flow field; they feel their direct, turbulent surroundings. As a result, they are continuously subjected to fluctuating forces. Estimates of the collection efficiency will strongly benefit from a detailed description of the development of these surroundings in time.

For these reasons, an attempt was undertaken to do numerical simulations with sufficiently high spatial and temporal resolution to be able to adequately resolve the four-dimensional (3-D space *and* time) nature of the single-phase flow field, including vortex-core precession.

Simulation procedure

Full resolution of the turbulent flow was virtually impossible. Although we simulated a downscaled model of a cyclone, operating at a moderate Reynolds number (14,000), the range of scales in the flow is too wide to be directly simulated. For this reason, a subgrid-scale model was applied. Subgrid-scale modeling, that is, large-eddy simulation, is a favorable approach to turbulence modeling in case of intrinsically unsteady flows (Eggels, 1996; Derksen and Van den Akker, 1999). As opposed to turbulence models based on the Reynolds-averaged Navier-Stokes (RANS) equations, large-eddy simulations (LES) clearly distinguish between the scales that are resolved, and the scales that are modeled. Therefore, as long as the resolution is sufficiently high to resolve them, coherent fluctuations (such as due to the PVC) are explicitly resolved by LES. In a RANS simulation, the turbulence model affects fluctuations at all scales, and therefore also coherent fluctuations. This would lead to the unwanted situation where turbulence models that are designed for turbulent fluctuations act on coherent fluctuations.

Next to the large-eddy approach to turbulence, the numerical setup we employed consisted of a lattice-Boltzmann discretization of the Navier-Stokes equations, and an adaptive force-field technique for part of the boundary conditions. This setup strongly resembles the one that was used successfully for simulating the turbulent flow in a stirred tank (Derksen and Van den Akker, 1999). The lattice-Boltzmann scheme was chosen for its (parallel) computational efficiency that is needed to reach the high spatial resolution required for LES.

This article serves two related purposes. The first is to present a numerical study that accurately resolves the three-dimensional, time-dependent flow in a reverse-flow cyclone, including vortex-core precession. To the best of our knowledge, this is the first report on the simulation of a PVC in a cyclone in a way that is consistent with experimental data. The second purpose is of a more generic nature, and is related to the use of large-eddy simulation for industrial flows as first presented by Eggels (1996) for stirred-tank flow. Here we (again) demonstrate that large-eddy simulations of flows in complex, practical geometries are feasible, have added value over RANS simulations, and can be run on relatively inexpensive, widely available computer platforms. This way, flow information with high spatial and temporal resolution becomes available. This information can serve as input for the transient modeling of a variety of transport processes (related to, for example, heat and mass transfer) encountered in industrial practice.

In the remainder of this article, first the flow geometry is introduced, then the numerical system is briefly treated. For a more extensive treatment, the reader is referred to Derksen and Van den Akker (1999), and to the other literature cited. In presenting the results, the emphasis will be on the comparison with measured velocity profiles, and on the spatial and temporal characterization of the precessing vortex core. Finally, some quantitative remarks are made on how to incorporate solid particles in the flow-simulation scheme.

Flow Geometry

The geometry of the flow system (see Figure 1) was dictated by the experimental study performed by Hoekstra et al., (1998a). Fluid is introduced tangentially into a cylinder, generating a strongly swirling flow. The exit pipe (also known as vortex finder) is a straight tube, which allows, the fluid to leave the cyclone through the top. The geometric swirl number Sw

$$Sw = \frac{\pi}{4}\frac{d_e D}{A_{in}} \tag{1}$$

(with D the diameter of the cyclone body; d_e the vortex finder's internal diameter; and A_{in} the cross-sectional area of the inlet) is a measure for the ratio of tangential-to-axial momentum (Gupta et al., 1984). From the dimensions in Figure 1, $Sw = 2.1$ can be calculated. For reasons of optical accessibility, the cyclone body was cylindrically shaped and had a flat bottom. This is in contrast to many practical cyclone designs (such as the design due to Stairmand; Stairmand 1951) that have conically shaped bodies. As we focus on the single-phase flow field, the geometry does not contain a particle outlet in the bottom region.

By means of laser Doppler anemometry (LDA), Hoekstra et al. (1998a) measured radial profiles of the average velocity, and of the rms velocity at several axial (that is, x-; see Figure 1) positions in the cyclone. Their LDA velocity time series revealed coherent fluctuations, whereas the precessing motion of the vortex core was visualized by means of a laser sheet technique. In the experimental study, the Reynolds number based on the superficial inlet velocity (U_{in}) and the cyclone body diameter, $Re = U_{in}D/\nu$, amounted to 15,000, whereas it was 14,000 in our numerical study. This is one to two orders of magnitude lower than the values at which industrial cyclones are operated.

The coordinate directions are defined in Figure 1. The origin of the coordinate system is located at the bottom of the cyclone, in its geometrical center.

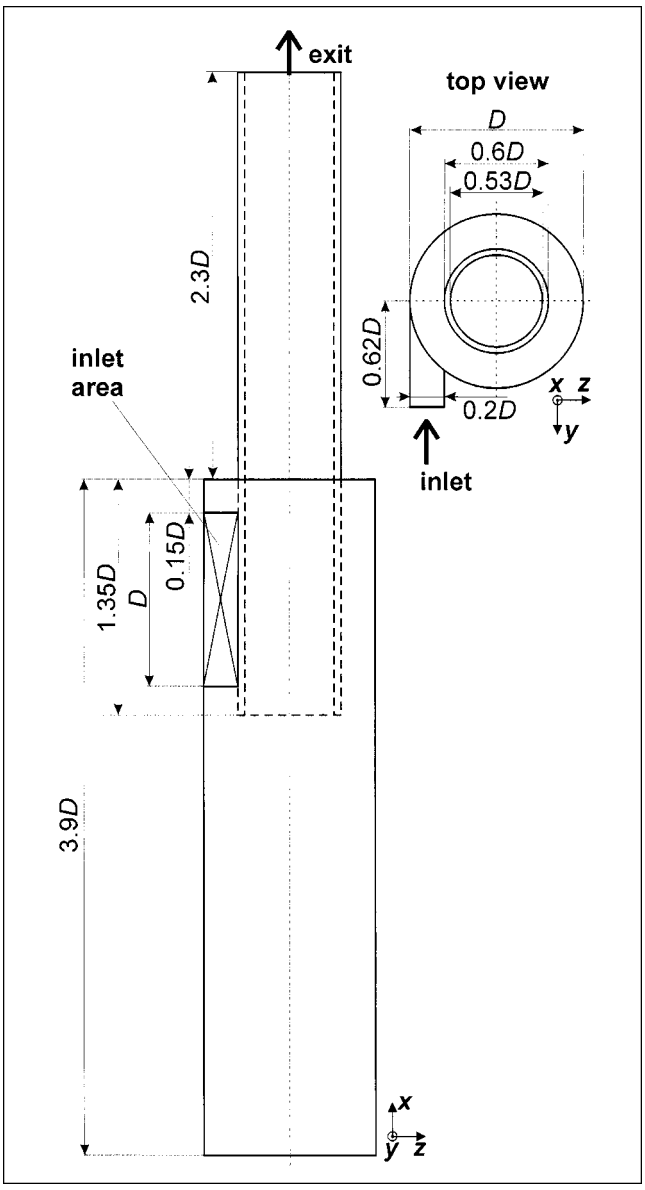

Figure 1. Flow geometry.

Numerical Setup

The Navier-Stokes equations were discretized by means of a lattice-Boltzmann scheme. Starting point for lattice-Boltzmann schemes is a many-particle system, residing on a lattice [in order to distinguish between the particles that constitute the lattice-Boltzmann scheme and the (to be collected) particles in the gas flow, we will refer to the latter from now on as ''solid particles'']. Every time step, the particles move to neighboring lattice sites, where they collide, that is, exchange momentum with all other particles involved in the collision. This simplified kinetic model for a fluid can be constructed in such a way that the macroscopic behavior of the system resembles a real fluid (Frish et al., 1986; Chen and Doolen, 1998). The specific scheme that is used in the present work is due to Somers and Eggels (Somers, 1993; Eggels and Somers, 1995). It differs slightly from the (*de facto* standard) lattice BGK models (Bhatnagar et al., 1954; Qian et al., 1992), in the sense that it explicitly takes the third- and some fourth-order terms into account. Subsequently, the third-order terms are effectively suppressed by the scheme.

The basic equation describing the evolution of the particle system in space x and t reads (such as Chen and Doolen, 1998)

$$N_i(x + c_i, t+1) = N_i(x, t) + \Gamma_i(N), \tag{2}$$

with N_i a particle mass in the ith lattice direction, c_i the discrete set of lattice vectors, and $\Gamma_i(N)$ the collision operator that depends on all particles (that is, the *vector* N) taking part in the collision. The density ρ and momentum concentration in the αth coordinate direction, ρu_α, are related to the sum of particle masses, and the distribution of mass over the various lattice directions, respectively:

$$\rho = \sum_i N_i \tag{3}$$

$$\rho u_\alpha = \sum_i c_{i\alpha} N_i. \tag{4}$$

With a proper choice of the collision operator Γ_i, and a lattice having the right symmetry properties (here we used a three-dimensional projection of a four-dimensional face-centered-hypercube lattice; see Somers, 1993), the continuity and (*almost*) the Navier-Stokes equations can be derived from Eq. 2 (Eggels and Somers, 1995). The deviations from the true Navier-Stokes equations only become negligible in the incompressible limit, that is, if the flow velocities are small compared to the speed of sound. In the present lattice-Boltzmann scheme $c_{\text{sound}} = 1/\sqrt{2}$ (in lattice units). In case the incompressible Navier-Stokes equations need to be simulated, this poses a severe restriction to the allowable velocities. In the simulation described here, velocity values did not exceed 0.15 lattice units (lu). A velocity in lattice units is a distance in terms of the lattice spacing traveled during a single time step.

The major reason for employing a lattice-Boltzmann scheme is its (parallel) computational efficiency. In classic incompressible flow simulations, the pressure satisfies a Poisson equation. Especially in complexly shaped flow domains, solution of this equation is numerically very expensive. Furthermore, due to the elliptic nature of the Poisson equation, in principle every grid point needs information from the entire flow domain. In a parallel, distributed-memory implementation, this adds quite a lot of communication overhead (Derksen et al., 1996). In contrast, the operations in the lattice-Boltzmann scheme only involve localized interactions. A distributed-memory lattice-Boltzmann program based on domain decomposition only requires communication of flow variables at subdomain boundaries, and therefore efficiently employs parallel resources.

A disadvantage, at least of the lattice-Boltzmann scheme we used, is its uniform, cubic lattice, which excludes local grid refinement. The latter certainly would have been a beneficial feature if the Reynolds number had been much higher. Here, due to the relatively low Reynolds number, boundary

layers are rather thick and can be adequately resolved by the uniform grid (see also the part of this section on wall-damping functions).

The cubic, or Cartesian, nature of the simulations posed more serious problems, as we needed to model cylindrically shaped walls. For this goal, an adaptive force-field algorithm, which was discussed in detail by Derksen and Van den Akker (1999), was employed. In the algorithm, the walls are viewed as forces acting on the fluid. At every time step, forces are calculated in such a way that they impose a prescribed velocity (zero velocity in the case of a static wall) at a large set of points that define the walls within the flow domain. These points do not necessarily need to coincide with lattice sites. Second-order interpolation was used to relate velocities and forces at lattice sites to the velocities and forces at the wall-defining points.

The forcing algorithm allows for a very simple and flexible way of incorporating complex geometries in the flow domain. A geometry is solely defined as a set of points on its surface. The distance between these points is typically one lattice spacing (or a bit less to avoid fluid flowing through the wall). Adaptation of the geometry, relevant for process optimization purposes, therefore only involves adapting the set of points defining it. The topology of the computational mesh is not affected by the adaptation.

For turbulence modeling, we employed the standard Smagorinsky subgrid-scale model (Smagorinsky, 1963). This is an eddy-viscosity model with a subgrid-scale eddy viscosity (ν_e) that is dependent on the local, resolved deformation rate:

$$\nu_e = \lambda_{\text{mix}}^2 \sqrt{S^2}, \tag{5}$$

with λ_{mix} the mixing length of subgrid-scale motion and S^2 the squared resolved deformation rate. The subgrid-scale stresses $\sigma_{\alpha\beta}$ amount to

$$\sigma_{\alpha\beta} = \nu_e \left(\frac{\partial u_\alpha}{\partial x_\beta} + \frac{\partial u_\beta}{\partial x_\alpha} - \frac{2}{3} \delta_{\alpha\beta} \nabla \cdot u \right), \tag{6}$$

with $\delta_{\alpha\beta}$ the Kronecker delta function. In the standard Smagorinsky model, the ratio between the mixing length λ_{mix} and the lattice spacing Δ is constant:

$$\lambda_{\text{mix}} = c_s \Delta. \tag{7}$$

A value of 0.1 was adopted for c_s (Piomelli et al., 1988). The implementation of the subgrid-scale model in the lattice-Boltzmann scheme is straightforward. In the collision phase, rather than the molecular viscosity ν, the total viscosity $\nu + \nu_e$ is used.

The proximity of a wall reduces the degrees of freedom for the turbulent eddies. As a result, turbulent fluctuations are damped. In terms of the Smagorinsky model, this implies that the mixing length needs to be reduced in the vicinity of a wall. This is not incorporated in the standard Smagorinsky model. Commonly, Van Driest wall-damping functions (Van Driest, 1956; Hinze, 1959) are applied for this goal:

$$\lambda_{\text{mix}} = c_s \Delta \left[\left(1 - \exp\left(- \frac{y^+}{A^+} \right) \right) \right], \tag{8}$$

with y^+ the dimensionless distance to the wall ($y^+ = (y u_* / \nu)$, and A^+ a constant equal to 26 (Van Driest, 1956). The parameter u_* is the local wall shear velocity: $u_* = \sqrt{\tau_w / \rho}$. In the simulations, we imposed a *uniform* value for the wall shear velocity. The boundary layer at the cyclone wall is mainly determined by the tangential velocity component. As a measure for the latter, the inlet velocity was taken. Subsequently we chose $u_* = 0.04 U_{in}$, in analogy to turbulent pipe flow where at $Re = 2 \cdot 10^4$, $u_* \approx 0.04 U_{\text{bulk}}$ (Hinze, 1959). Also based on these assumptions, the lattice spacing can be calculated in terms of wall units (Δ^+): $\Delta^+ \equiv (\Delta u_* / \nu) = 7.5$. The latter value implies that the resolution of the simulations is sufficiently high to resolve the boundary layer.

Implementation

A grid consisting of uniform, cubic lattice cells was defined. In the axial direction it was 499 lattice units (lu) long. The size in the two lateral directions was 99 lu. In this block of cells, the surface of the geometry as defined in Figure 1 was represented by a set of 247,334 points. Their nearest-neighbor spacing varied between 0.7 lu and 1.0 lu. The diameter of the body of the cyclone in terms of the grid spacing was 80 lu. The other dimensions of the cyclone can be derived with the help of Figure 1.

Apart from the no-slip boundary conditions at solid walls, an inlet and outlet needed to be defined. The rectangular inlet area was 80 lu in the axial direction and 16 lu in the lateral direction. At the inlet nodes, the forcing algorithm was used to impose a uniform inlet velocity $U_0 = 0.07$ lu, except for the velocities at the perimeter of the inlet area that were set to $0.7 \cdot U_0$. As a result, the (superficial) inlet velocity U_{in} amounted to 0.067 lu. With respect to the (lattice-Boltzmann) particles entering the flow domain at the inlet, a zero-gradient condition in the flow direction was applied. The latter boundary condition was also applied at the outlet of the cyclone, that is, at the end of the exit pipe.

A zero-velocity field was defined as the initial condition. In order to limit the computational effort for reaching a quasi steady state, first the flow in a cyclone with a short body ($H = 2D$, instead of $H = 3.9D$) was simulated. When this flow system was more or less developed, the length of the body was gradually increased by copying flow-field values in horizontal planes to new axial positions.

The computer codes for executing the simulations was implemented on two different parallel computer platforms: (1) a HP-Convex S-Class parallel computer, equipped with four processing units and a (shared) memory of 1 Gbyte, and (2) a cluster of two Dual Pentium II systems with 1 Gbyte of memory each, connected through a 100-Mbit/s network switch. Parallelization was performed by means of domain decomposition, that is, the computational domain was divided into subdomains that communicate flow values at subdomain boundaries by means of a message passing tool (PVM, in this case). The total memory requirements were about 0.6 Gbyte.

The wall-clock time per time step for the code running on a single processing element typically was 30 s on either platform. Simulation of a single integral time scale (defined here as D/U_{in}) therefore requires 10 hours wall-clock time. Parallel implementations, however, can reduce this time drastically. Running the code on the four processing elements gave wall-clock time reductions with a factor of 3.8 or more on either platform. A similar code has also been implemented on a SGI Origin 2000 computer with 20 processing elements. A twelve-way run revealed the superlinear speed-up number of 13.

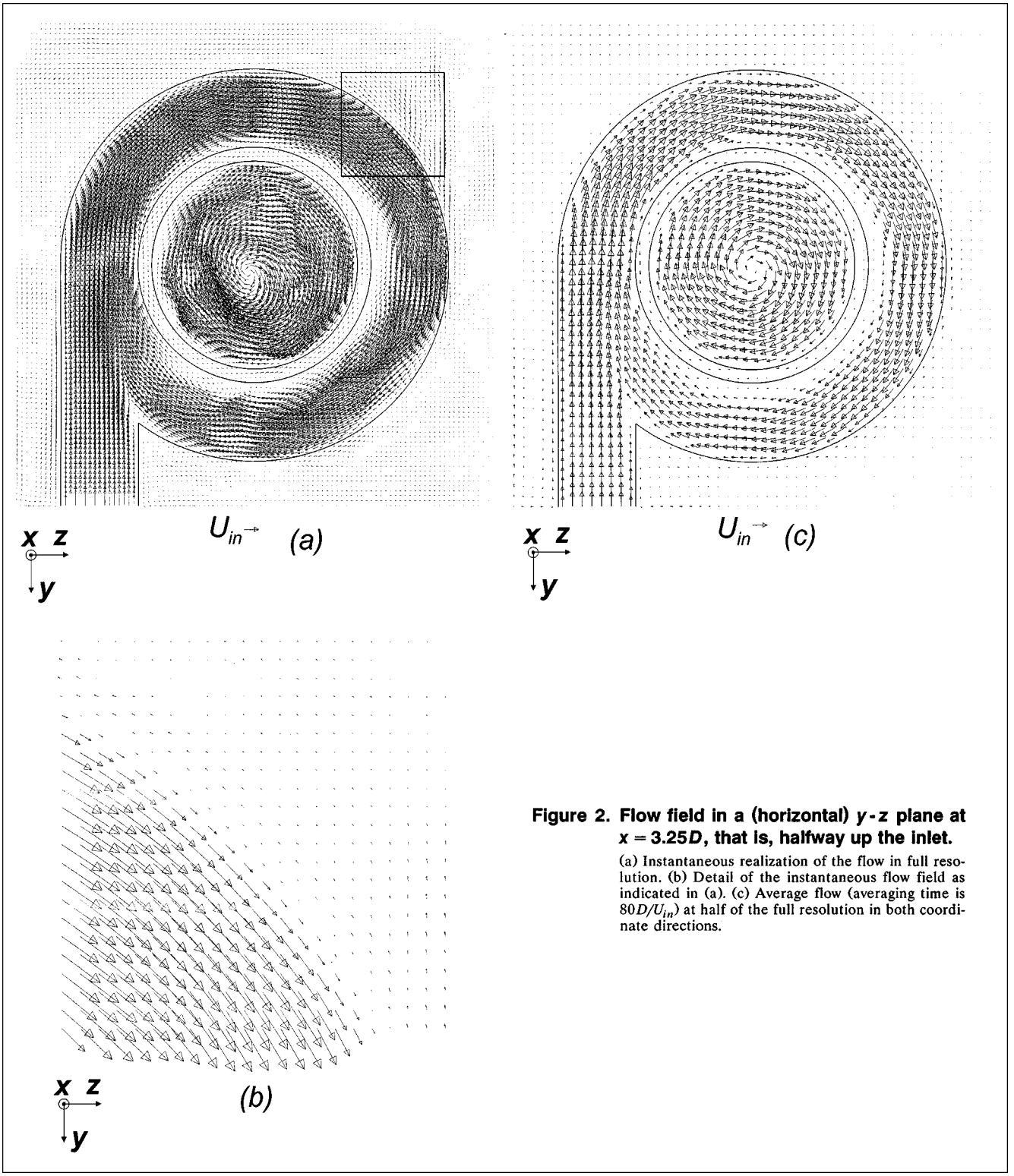

Figure 2. Flow field in a (horizontal) y-z plane at $x = 3.25D$, that is, halfway up the inlet.

(a) Instantaneous realization of the flow in full resolution. (b) Detail of the instantaneous flow field as indicated in (a). (c) Average flow (averaging time is $80D/U_{in}$) at half of the full resolution in both coordinate directions.

Therefore, the procedure opens the possibility to relatively cheaply and flexibly run large-scale simulation applications.

Results

General impressions of the flow field

The way the swirling motion is generated by the tangential inlet is shown in Figure 2. Figure 2a is a snapshot of the flow at inlet level, whereas Figure 2c shows the average flow. In Figure 2, the full horizontal flow domain is depicted, that is, including the lattice cells that fall outside the cyclone geometry. The solid lines and curves in the figure represent the walls that are defined by means of adaptive forces. The detail (Figure 2b) qualitatively shows that a curved wall can be implemented this way in the cubic grid without generating a staircase-like boundary. From Figure 3 on, only internal flow-field results will be presented, that is, the (virtual) flow outside the cyclone geometry is not taken into account.

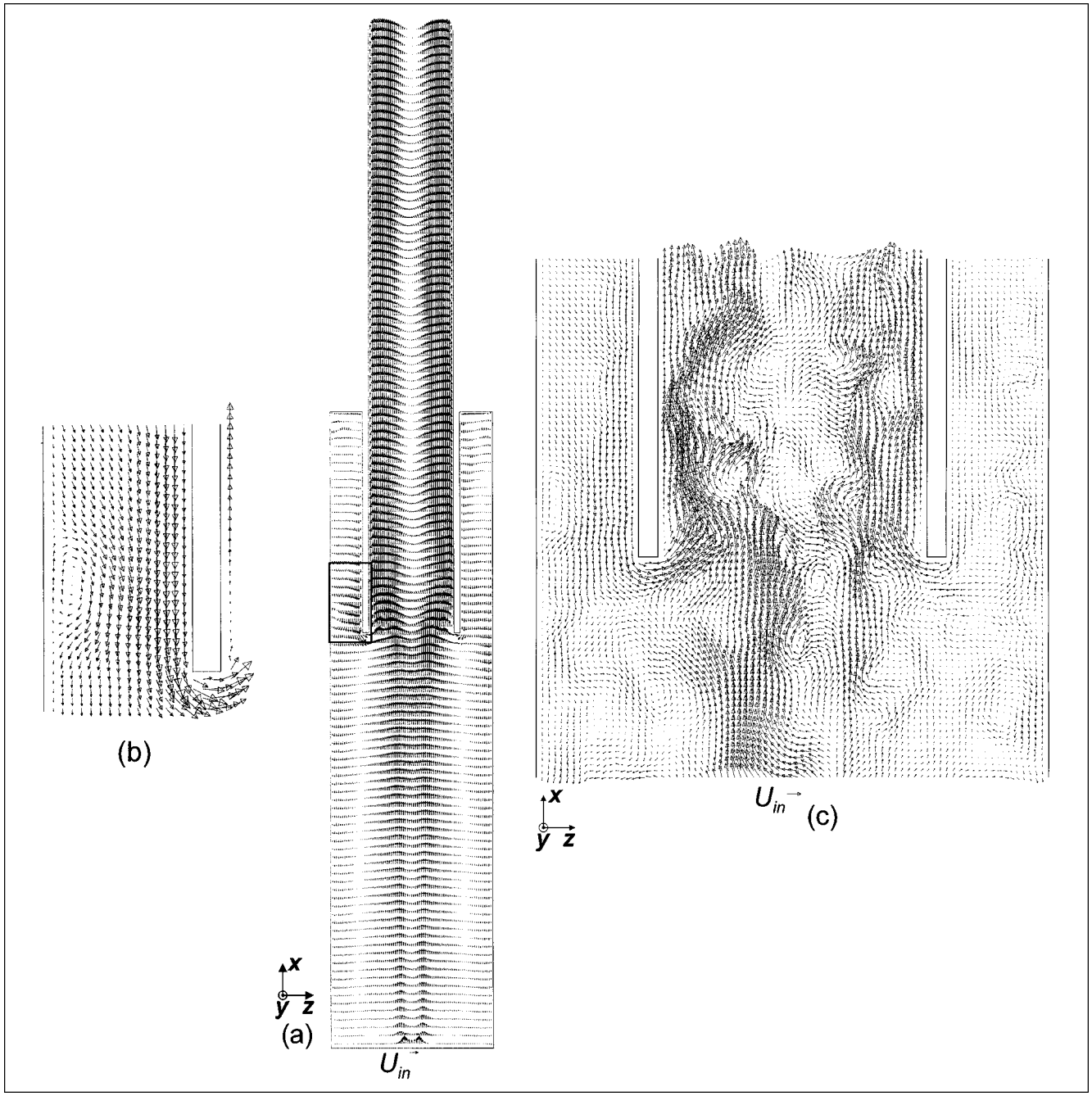

Figure 3. Flow field in the (vertical) x-z plane through the center of the cyclone body (at $y = 0$).

(a) The average flow field. The averaging time amounted to $80\,D/U_{in}$. Every fourth vector in x-direction is drawn. (b) Detail of the average flow, showing the recirculation and the enhanced shortcut flow it induces. (c) Detail of the instantaneous flow in the entrance region of the vortex finder. This image gives the full resolution of the simulations.

It can be observed that in the region where the inlet flow merges with the annular flow, fluid coming from the inlet is being accelerated. Starting approximately at the one o'clock position of Figure 2a, a flow separation zone at the inner wall of the annulus is present. This zone, which extends over some 180°, has low tangential velocity and even flow reversal. On average (see Figure 2c) there is no reversal. There is indirect experimental evidence for the presence of this low-speed zone at the inlet level, as it has been observed in industrial cyclones that solid particles tend to accumulate at the parts of the inner wall of the annulus that more or less correspond to the simulated region of separation.

The snapshot shows an off-axis vortex core within the vortex finder, whereas on average (Figure 2c) the core is close to the cyclone's geometrical center. This is the first indication of the presence of vortex-core precession in the simulations. The preceding observations on the horizontal flow field in the inlet region clearly indicate an angular dependence of the flow variables. An axisymmetric simulation cannot capture this dependency.

The average flow field in a vertical plane is given in Figure 3a. Some global observations can be made. The (radial) profiles of axial velocity in the cyclone body show a complicated structure, with downflow near the wall, upflow in the inner region, and a strong velocity deficit near the center. The latter is a well-known feature for strongly swirling flows (such as Escudier et al., 1980). Also the flow in the vortex finder exhibits this deficit. Furthermore, there is a shortcut flow at the bottom of the vortex finder, that is, some fluid hardly enters the cyclone body, but is almost directly sucked into the exit pipe. Solid particles within this shortcut flow will only very briefly experience a centrifugal field and particle separation will be hampered. An interesting flow detail is the recirculation near the cyclone body wall, just downstream from the inlet (see the detail, Figure 3b). This recirculation is also present in the snapshot of the flow (Figure 3c), although here it is obscured by all kinds of eddies. The recirculation is due to the separation, at the end of the inlet pipe, of the boundary layer attached to the lower wall of the inlet pipe. The recirculation bubble forces fluid coming from above in an inward direction, thereby enhancing shortcut flow (note that due to the recirculation, the shortcut flow at the left side in Figure 3a and 3c is much stronger than at the right side). The turbulent nature of the flow is evident from Figure 3c. Gradients are very high at the entrance of the vortex finder. Also the velocity deficit in the center of the vortex finder can be clearly observed. The vector field in the vortex finder shows a qualitative resemblance with the field measured by Griffiths et al., (1998), albeit that they were measured just above the cyclone's exhaust.

In order to apply Van Driest's wall-damping functions (Eq. 8), an assumption regarding the wall shear velocity (that is, $u_* = 0.04U_{in}$) was made. Once the simulations were performed, this assumption could be tested. It was found that the time-average wall shear velocity varied slightly throughout the cyclone. At the inner wall of the vortex finder, average values of approximately $0.03U_{in}$ were encountered. The wall region that presumably is having the most impact on the overall flow field is at the cyclone body inner wall. Here, $u_* \approx 0.03U_{\text{in}}$ near the top. This gradually decreased to $u_* \approx 0.02U_{\text{in}}$ near the bottom. In conclusion, the assumption of a constant wall shear velocity throughout the geometry seems to be a fair one. Furthermore, a slightly too high value of the

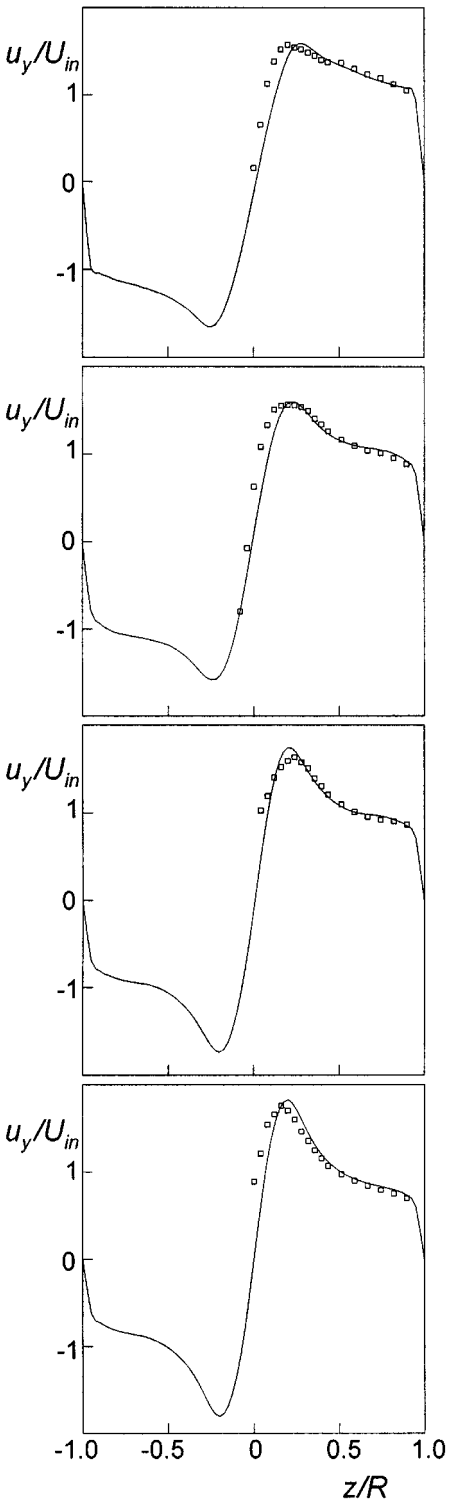

Figure 4. Radial profiles of the average tangential velocity at four axial positions.

From bottom to top: $x/D = 0.89$, 1.39, 1.89, and 2.39. The curves represent the simulations. The symbols are the experimental values by Hoekstra et al. (1998a).

wall shear velocity was used in the wall-damping function ($0.04U_{in}$ instead of 0.02 to $0.03U_{in}$). It is believed that this deviation has no significant impact on the main flow-field results.

Comparison with LDA experiments

In order to judge the quality of numerical simulations, experimental data are inevitable. In the present article, the experimental evidence is mainly extracted from a study performed in our laboratory by Hoekstra et al. (1998a). The experimental geometry and flow conditions were almost fully represented by the large-eddy simulations. The exceptions being the inlet that was shorter in the simulations and was having a well-defined velocity profile (that is, there was no turbulence introduced at the inlet), and the exit pipe that had a zero-gradient boundary in the simulations, whereas in reality it blew into free space.

Among other things, velocity profiles were measured at four axial positions (that is, at $x/D = 0.89$, 1.39, 1.89, and 2.39) by means of LDA. At each axial location, the measurement volume was traversed in the z-direction (see the coordinate system defined in Figure 1), over a line through the cyclone body's geometrical center, starting close to the wall (that is, at $z/R \approx 0.9$, with $R = D/2$) and ending at, or slightly opposite to the center. Average velocities and rms velocity values were derived from the measured-velocity time series. Only the tangential (that is, y) and axial (that is, x) velocity components were measured.

Figures 4 and 5 show the measured average values, along with the corresponding simulation results. The averages in the simulations were gathered over a run that extended over a time period of $80D/U_{in}$. The agreement regarding the mean tangential velocity (Figure 4) is good. The maximum level of tangential velocity is predicted very well by the simulations. This is also true for the axial development of the tangential velocity profiles. Closer to the bottom of the cyclone, the decay of tangential velocity toward higher radii in the free vortex region is much stronger than higher up in the cyclone. The major deviation is related to the solid body rotation in the cyclone's center. The experiments clearly show a higher slope than the simulations, that is, in reality, fluid in the cyclone core rotates faster than was simulated.

The latter effect might be related to the mismatch between experiment and simulation of the axial velocity near the center of the cyclone (see Figure 5), especially at the upper two profiles. Here, the simulated velocity deficit at the axis is much weaker than its measured counterpart. Apart from this, the profiles of experiment and simulation agree well. Some experimentally observed details, such as the "shoulders" in the axial velocity profiles, are present in the simulations as well.

The rms profiles (Figures 6 and 7) show complicated features. Near the center, rms values are (much) higher than close to the wall. This very likely can be attributed to the PVC, as the rms profiles reflect some features of the (gradients) in the *average* velocity profiles. This effect was also observed by Hoekstra et al. (1998b) in an experimental study, albeit for a different cyclone geometry.

First the simulated tangential rms velocity profiles (Figure 6) will be discussed. The maximum rms values are observed at the center. Here, most of the fluctuations' intensity is due to the vortex core moving with respect to the stationary ob-

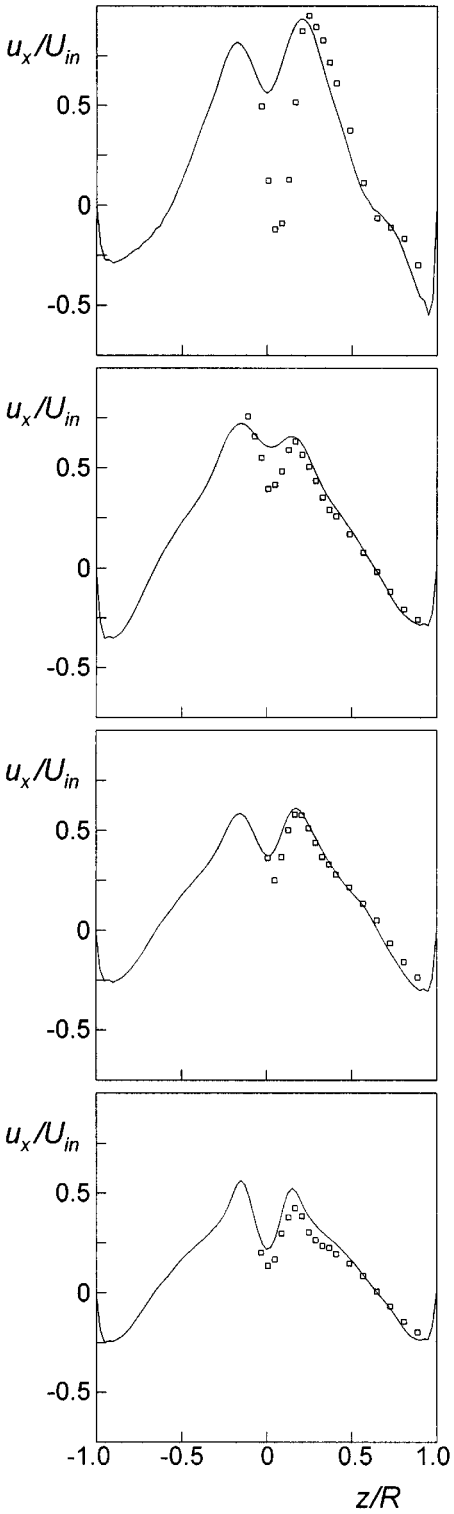

Figure 5. Radial profiles of the average axial velocity at four axial positions.

From bottom to top: $x/D = 0.89$, 1.39, 1.89, and 2.39. The curves represent the simulations. The symbols are the experimental values by Hoekstra et al. (1998a).

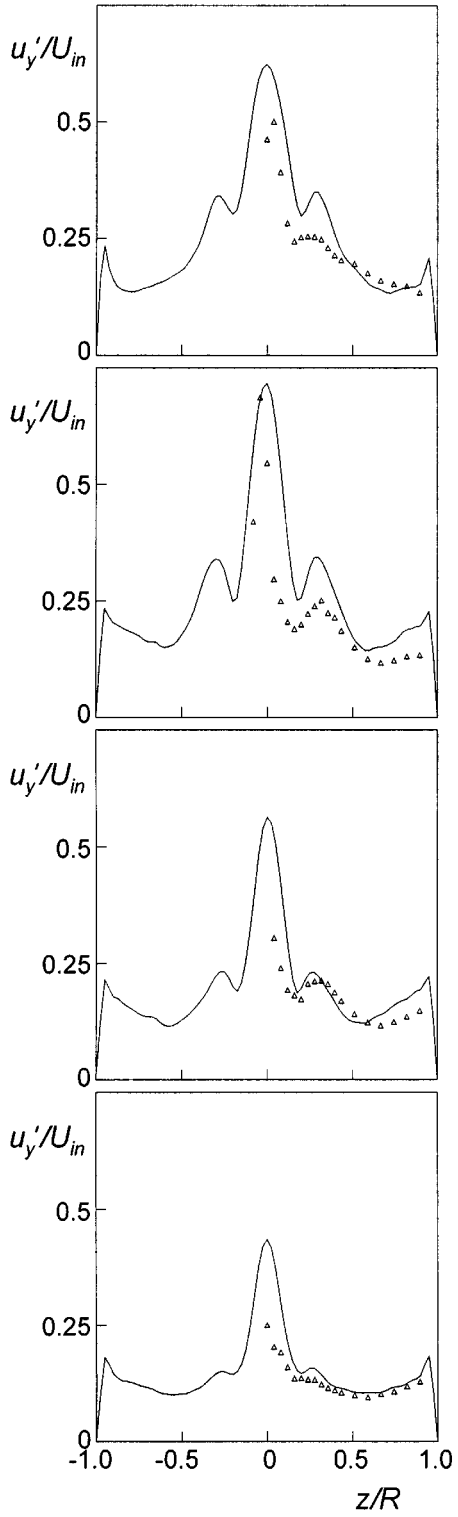

Figure 6. Radial profiles of the tangential rms velocity at four axial positions.

From bottom to top: $x/D = 0.89$, 1.39, 1.89, and 2.39. The curves represent the simulations. The symbols are the experimental values by Hoekstra et al. (1998a).

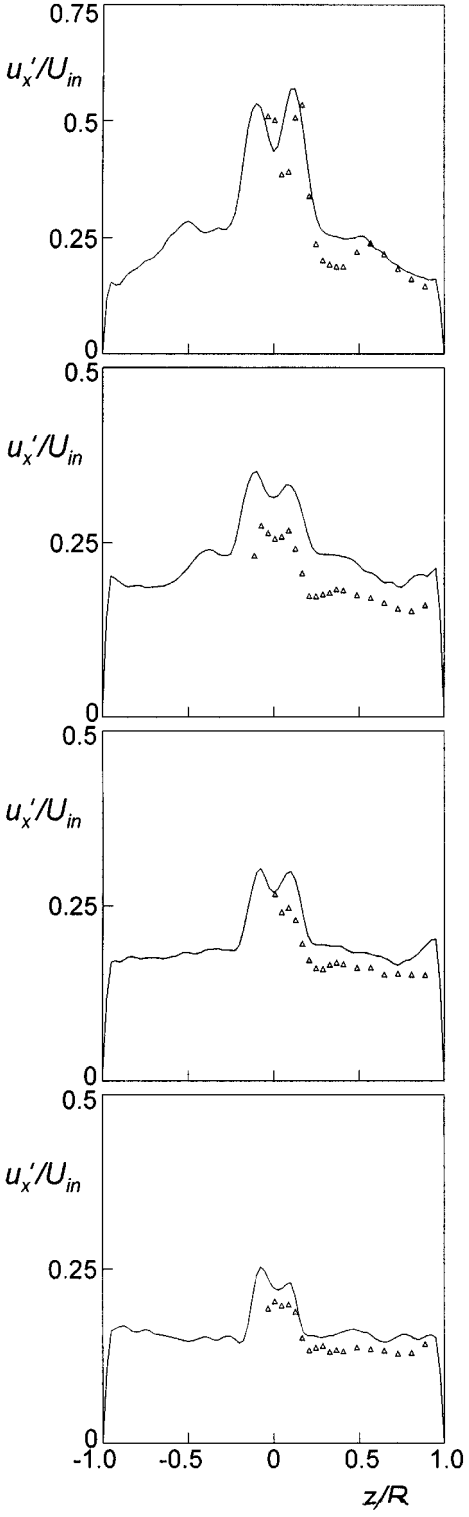

Figure 7. Radial profiles of the axial rms velocity at four axial positions.

From bottom to top: $x/D = 0.89$, 1.39, 1.89, and 2.39. The curves represent the simulations. The symbols are the experimental values by Hoekstra et al. (1998a).

server. In combination with the high tangential velocity gradients, vortex-core motion results in high fluctuation levels. Vortex core precession also explains the local minima in the fluctuating tangential velocity at either side of the maximum.

At the radial positions of the minima, the mean velocity profile has a zero gradient. As a result, vortex-core precession does not induce much fluctuation. Outside the core region, turbulence dominates the fluctuations, with a slightly increased turbulence intensity level in the wall layer, which has also been observed in turbulent channel flow (such as Kim et al., 1987). Qualitatively, the experiments show the same features, although the limited number of experimental points and (more importantly) the limited span of the experiments (no data available at the other side of the center) impairs a detailed comparison. Quantitatively, the simulations slightly overpredict the levels of fluctuation.

Also the axial rms velocity in the core region can be related to vortex-core precession and the shape of the mean axial velocity profile. The latter has a zero gradient at the center, which is reflected in the rms profiles as a local minimum at $z/R \approx 0$ (Figure 7). Due to the less strong gradients of the axial velocity profiles, compared to the tangential profiles, rms values of the axial velocity in the core region are much lower than tangential rms values. In the outer region, however, the levels of axial and tangential rms values are comparable. As was also observed for the tangential component, the simulations tend to slightly overpredict the axial rms velocities.

Vortex-core precession

The effect of the PVC on the levels of the velocity fluctuations was already discussed in the previous section. In this section we present a phenomenology of the vortex-core precession as it has been simulated, along with a comparison with some experimental data.

In an experiment, vortex-core precession manifests itself as a (quasi-) periodically fluctuating signal, for example, a pressure or velocity signal. Figure 8a gives a *simulated* velocity signal. Clearly its (quasi-) periodic nature can be observed. The corresponding spectrum (Figure 8b) exhibits a peak at $f_{\text{peak}} = 0.53U_{\text{in}}/D$. The Strouhal number $St = (f_{\text{peak}} D/U_{\text{in}})$ then amounts to $St = 0.53$. This is in good agreement with the experimental value of $St = 0.49$ (Hoekstra et al., 1998a).

In Figure 9, the vortex-core precession has been visualized by means of the pressure field in a horizontal plane about halfway the cyclone body. The core of the vortex can be associated with the point of least pressure. According to Figure 9, this pressure minimum moves about the cyclone center with an amplitude of the order of 0.1 times the cyclone diameter. Furthermore, in the contour plots two clearly different flow regions can be distinguished: the inner and outer regions. The outer region is turbulent. In this region, structures are formed from time to time in a seemingly erratic manner. The inner region, that is, the region close to the pressure minimum, behaves much more deterministically. Here, the shape of the contour lines only changes gradually. By choosing a different gray-level scale (see Figure 10), the relative dimensions of the inner and outer regions are estimated. Roughly at $r_c \approx 0.31R$, with R the cyclone body radius, a caesura line can be drawn. The inner region identified this way is slightly larger than the forced vortex region (see Figure 4). The radial position of the maximum tangential velocity, which is generally taken as the outer boundary of the forced vortex, is $r_f \approx 0.25R$ at $x/D = 1.89$. Apparently, the forced vortex stabilizes the flow. This is

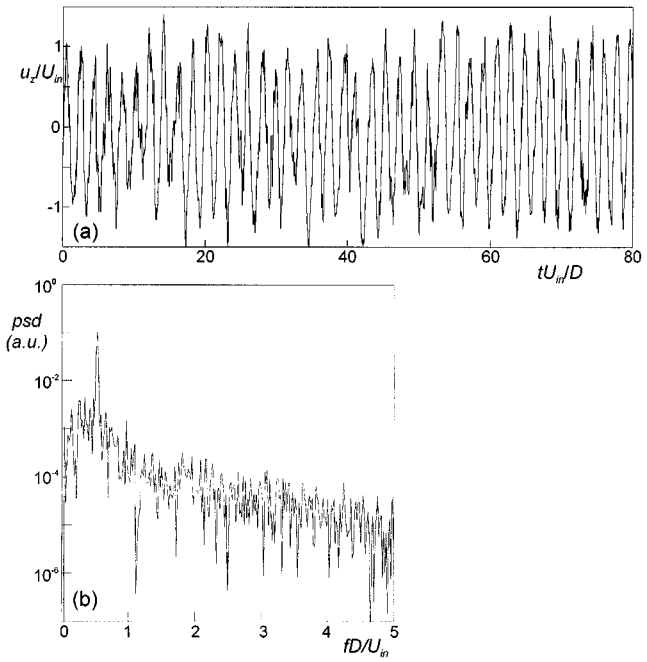

Figure 8. (a) Time series of the velocity component in the z-direction at $x/D = 1.9$, $y = 0$, $z = 0$; (b) the corresponding power spectral density function.

a well-known feature of swirling flow (such as flames are stabilized by swirl, Gupta et al., 1984). Also in cyclones there is experimental evidence for the phenomena observed. In a joint LDA and LIF (laser-induced fluorescence) study in a re-

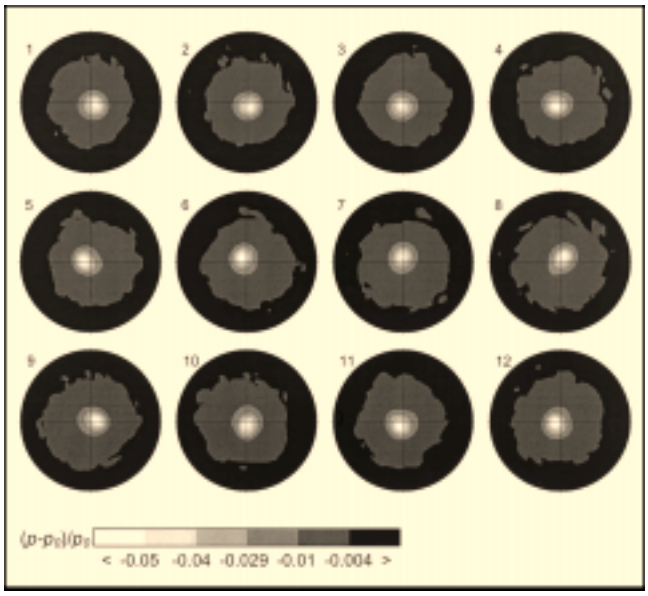

Figure 9. Twelve realizations of the pressure field in the horizontal plane at $x/D = 1.9$.

The time spacing between the subsequent images is $0.19D/U_{\text{in}}$, that is, approximately one-tenth of the average vortex-core precession period.

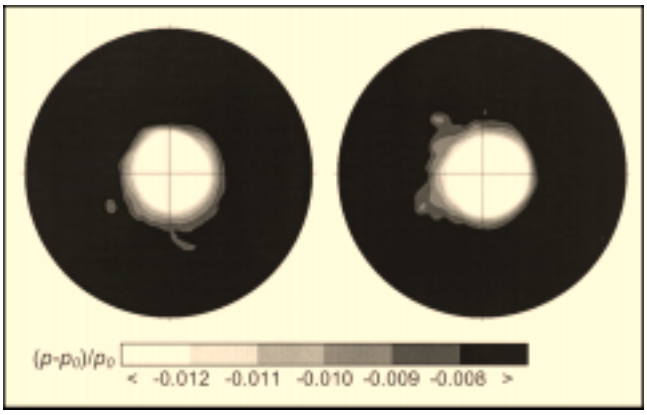

Figure 10. Two randomly picked realizations of the pressure field in the horizontal plane at $x/D = 1.9$.

versed-flow cyclone by Fokke et al. (1994), it was demonstrated that turbulent mixing in the radial direction is almost absent in the forced vortex, whereas it is very strong in the free vortex.

Surprisingly, however, the eddy viscosity, as calculated according to Eq. 5, does not seem to feel the distinction between forced and free vortex. Apart from the wall regions, ν_e is distributed fairly uniformly throughout the cyclone, having values of typically 0.8 to 1.1 times the molecular viscosity. The eddy viscosity not reacting on the forced vortex is probably due to the isotropic nature of the Smagorinsky model. The model cannot represent the anisotropy introduced by swirl. We speculate that this shortcoming is (partly) the cause of the deviations from experimental data we observed in the core regions with respect to the average velocity profiles (Figures 4 and 5). There, the gradients of the tangential velocity component as well as the axial velocity deficit were significantly under predicted.

During the same time interval as in Figure 8, the position of the vortex core at the axial location $x/D = 1.9$ (that is, at approximately halfway the cyclone body) was recorded every time step. The core's position was derived from the pressure field: the lattice cell in the selected horizontal plane having least pressure was located. Then, by means of a parabolic fit, the position of the pressure minimum at sublattice level was determined. The vortex-core path was obtained in this way. It is plotted in Figure 11a. At this axial position, the probability density functions (pdfs) for the y- and z-position of the vortex-core location (see Figure 11b and 11c) both have first moments close to zero, and a standard deviation of $0.070R$ and $0.068R$, respectively. The vortex core seems to avoid the cyclone's center, as can be seen from the pdf of the radial position (this pdf has been normalized for the bin area, which is proportional to the radius) of the vortex core (Figure 11d). The pdf peaks at $0.07R$. The vortex core does not seem to have a preferred angular position (Figure 11e).

Finally, we consider the development in the axial direction of the vortex-core precession (see Figures 12 and 13). The time-averaged position of the vortex does not strongly deviate from the geometrical center of the cyclone, with the exception of the entrance region of the vortex finder. Here the average vortex-core location with the highest radial value is found: at $x/D = 2.6$ (that is, just below the vortex finder) $\overline{r_{vcp}} = 0.03R$. The vicinity of the inlet, which is a region with the most geometrically imposed nonaxisymmetry, probably causes this. In the vortex finder, the core appears to be more strongly off-axis than in the cyclone body.

The rms values of the y- and z-coordinates of the vortex-core position are generally much larger than the average values (see Figure 13). The fact that the curves for the y- and z-coordinates almost coincide implies the absence of a directional preference of the vortex core. As for the average location, the most interesting region is the entrance of the vortex finder. Here, a clear peak in the rms values is observed. There is one experimental data point that can be directly compared with the simulation results: Hoekstra et al. (1998a) visualized the vortex-core motion by seeding the cyclonic flow with tracer particles and illuminating a horizontal plane at $x/D = 1.0$ with a laser sheet. Light scattered by the tracers was recorded through the bottom of the cyclone with a CCD camera. This way, the position of the vortex core could be clearly distinguished as a dark spot, that is, spot with the least concentration of tracer particles. The standard deviations of the measured pdfs in the y- and z-directions, were $0.024R$ and $0.018R$, respectively. The simulated values were $0.031R$ for the y- as well as the z-coordinate.

Consequences for solid-particle transport

For the application of the present simulation scheme to collection efficiency predictions, the fluid-flow algorithm needs to be extended with a method that describes how solid particles are transported through the cyclone. Generally speaking, two approaches can be distinguished. In the first approach, particles are released in the flow field, and their trajectories are calculated (Euler-Lagrange). In the second approach, the particulate phase is treated as a second continuum (Euler-Euler). Here, we briefly explore the possibilities and limitations of an Euler-Lagrange approach.

Two distinct issues need to be addressed. The first is related to individual solid particles, and to what extent they are subject to the resolved flow fluctuations on one side, and the (modeled) subgrid-scale fluctuations on the other. The relevant parameter here is the particle's relaxation time. The second issue is the way the solid particles modulate the gas flow field. The strength of the modulation is mainly governed by the particle volume fraction ϕ_v, and the density ratio of the continuous and dispersed phases (Elgobashi, 1994).

The relaxation time (T_p) of a solid particle in a gas stream is the time required for the particle to adapt itself to changing flow conditions. In other words: the fluctuations in the flow field with a frequency much higher than the inverse particle relaxation time are hardly felt by the particle, whereas the particle can easily adapt itself to frequencies much lower than the inverse relaxation time. For a spherical solid particle experiencing Stokes drag:

$$T_p = \frac{1}{18}\frac{\rho_p}{\rho}\frac{d^2}{\nu}, \tag{9}$$

with ρ_p and ρ the solid particle and gas density, respectively, and d the solid particle diameter. The maximum (cutoff) fre-

quency f_{co} of the fluctuations in the resolved flow field can be estimated to be of the order of $f_{co} = U_{in}/\Delta$, which approximately amounts to $100U_{in}/D$. For comparison of f_{co} with the solid-particle frequency T_p^{-1}, we need the assign physical dimensions to the simulated cyclone. For its diameter D we take 0.4 m, and for its inlet velocity, $U_{in} = 8\ \mathrm{ms}^{-1}$. If we further assume a density ratio $\rho/\rho_p = 10^{-3}$, and a kinematic viscosity $\nu = 2 \cdot 10^{-5}\ \mathrm{m}^2 \cdot \mathrm{s}^{-1}$, the cutoff frequency f_{co} typically

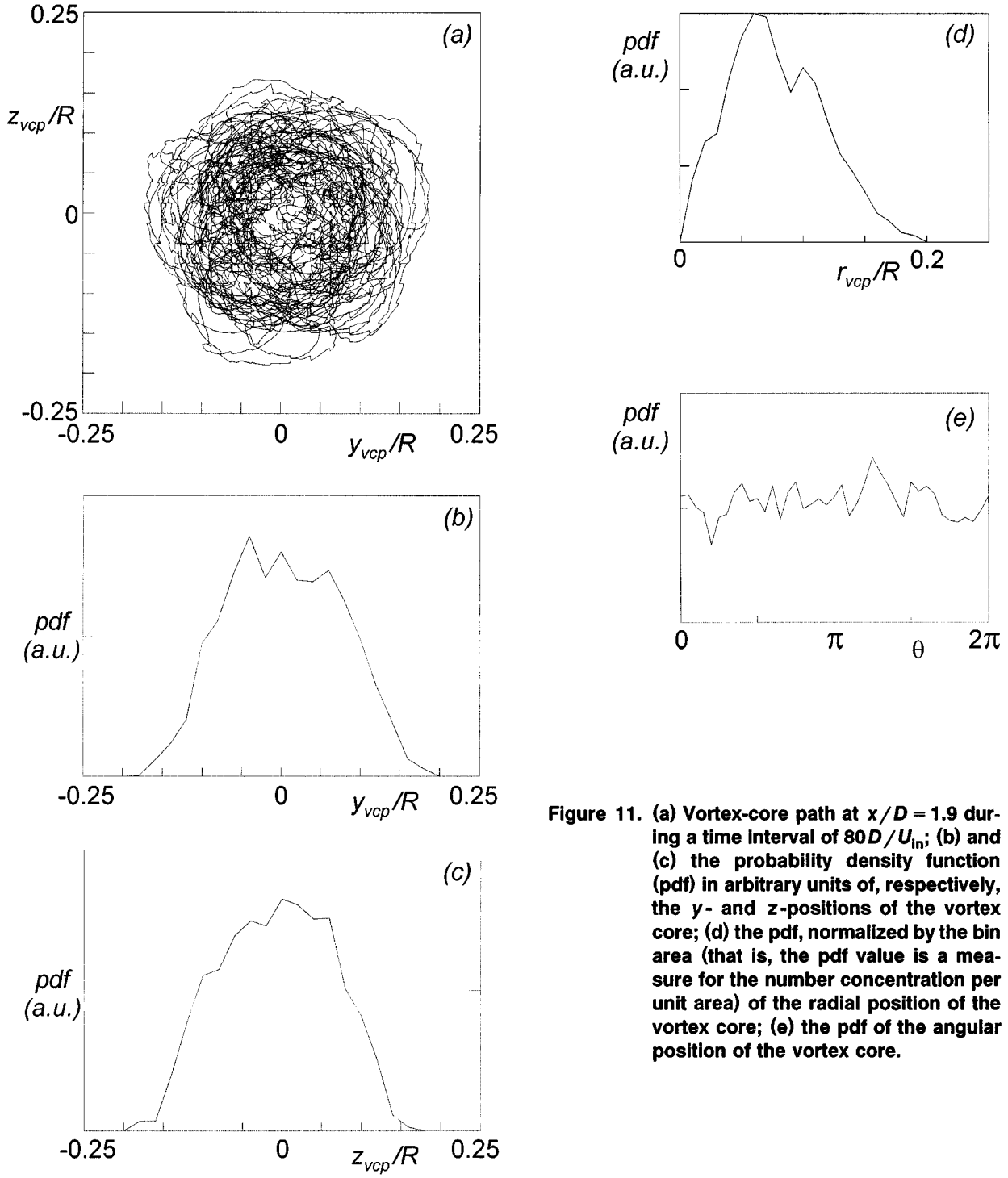

Figure 11. (a) Vortex-core path at $x/D = 1.9$ during a time interval of $80D/U_{in}$; (b) and (c) the probability density function (pdf) in arbitrary units of, respectively, the y- and z-positions of the vortex core; (d) the pdf, normalized by the bin area (that is, the pdf value is a measure for the number concentration per unit area) of the radial position of the vortex core; (e) the pdf of the angular position of the vortex core.

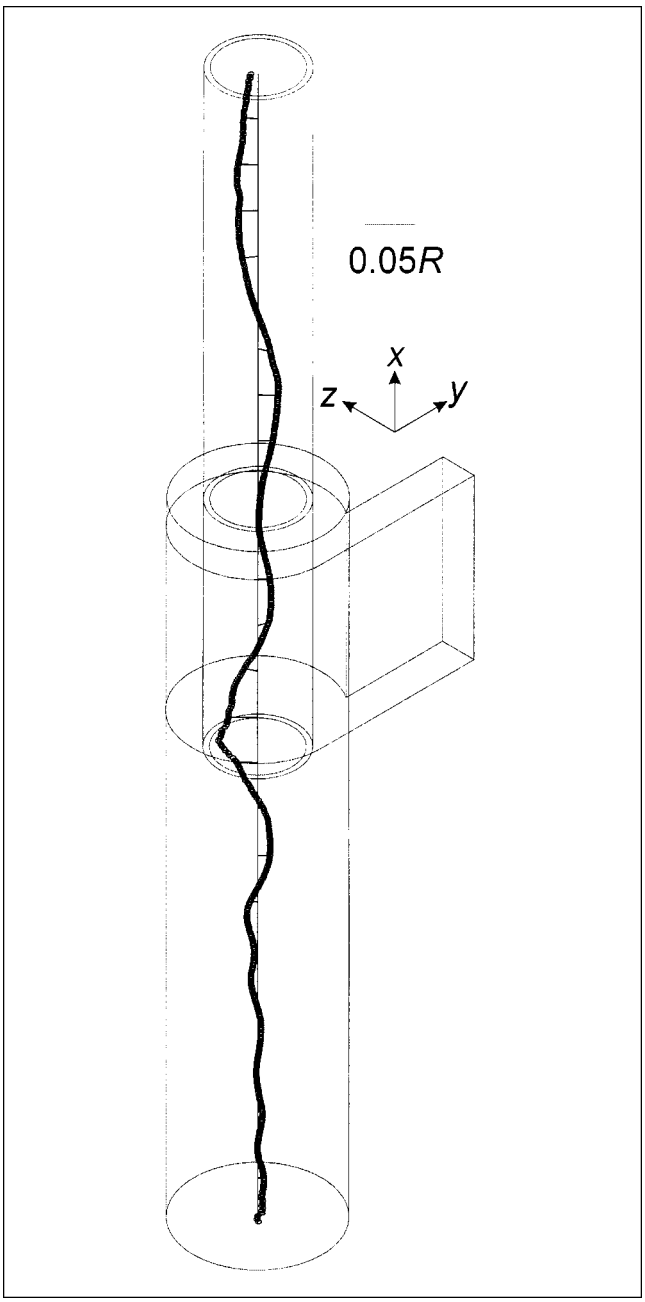

Figure 12. Average vortex-core position throughout the cyclone.

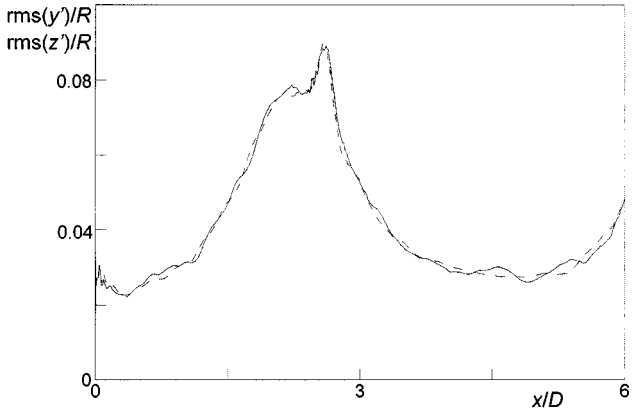

Figure 13. Root mean square of the *y*- and *z*-coordinate of the vortex core position as a function of the axial location.

With $x/D = 0$ and $x/D = 6$ corresponding to the bottom of the cyclone, and the exhaust respectively. The solid curve represents the *y*-coordinate, the dashed curve the z-coordinate.

corresponds to a 10-μm particle. This implies that modeling solid-particle trajectories with particle sizes larger than 10 μm does not require any assumptions regarding turbulent fluctuations, that is, for the particle, relevant surroundings are fully resolved by the LES. Solid particles smaller than 10 μm in diameter feel the subgrid-scale fluctuations. As a result, for such particles a stochastic process needs to be incorporated in the simulation scheme to model the effect of the subgrid-scale motion. It should be noted, however, that the assumptions that govern such a stochastic process are less speculative, and that the process itself is less influential compared to the stochastic processes that need to be designed to incorporate the action of turbulence in a particle tracking routine based on a RANS flow field.

At the conditions just defined, a 10-μm solid particle has a relaxation time of $0.01 D/U_{in}$. This is much smaller than the time scale associated with vortex core precession ($1.9 D/U_{in}$). As a consequence, the solid particle can easily follow the fluctuations induced by the precession. Collection efficiency will therefore not be influenced directly by the PVC. However, there might be an indirect influence through a nonlinear coupling between flow scales (that is, an energy cascade mechanism).

The mass loading $\phi_m = \phi_v\ (\rho_p/\rho)$ in cyclones strongly depends on the application, and can vary from values well above 1 to 10^{-4} (Hoffmann et al., 1992). For instance, the latter values are encountered in high-efficiency cyclones for the separation of small (1–10 μm) particles. If the solid particle concentration is very low, the influence the particles have on the flow field can be neglected. This is known as one-way coupling. In the case of higher concentrations, the turbulence will be modulated by the presence of the particles, and the flow and the particle trajectories need to be solved simultaneously (two-way coupling). At even higher mass loadings, particle–particle collisions need to be taken into account. According to Elgobashi (1994), the solid-particle volume fraction ϕ_v and the density ratio ρ/ρ_p determine the relative importance of the different coupling mechanisms. At $\rho/\rho_p = 10^{-3}$, and ϕ_v less than 10^{-6}, the influence of small solid particles on the turbulence is negligible. For volume fractions between 10^{-6} and 10^{-3}, two-way coupling becomes important. At higher volume fractions, particle–particle collisions need to be taken into account.

As a result, one-way coupling can be applied safely in high-efficiency cyclones. This has the great advantage that the number of solid particles that need to be processed is very limited. The only criterion is the statistical convergence of the value of the separation efficiency. Typically 10^4 particles are required per solid particle size class. If two-way coupling is at stake, for example, at $\phi_v = 10^{-6}$, and with $d = 10^{-5}$ m

and $D = 0.4$ m, the number of solid particles in a *single lattice cell* is approximately 100. As this is large compared to the 18 lattice-Boltzmann particles per cell, the particle tracking will become computationally more expensive than the fluid-flow simulation. For larger particles ($d \geq 2 \times 10^{-5}$ m), the number of solid particles per lattice cell decreases quickly and two-way coupling simulations based on an Euler-Lagrange framework become feasible.

Conclusions

The single-phase flow field in a reverse-flow cyclone has been modeled numerically. In order to sufficiently resolve the flow, and in particular the experimentally well-known phenomenon of vortex-core precession, a three-dimensional simulation procedure with high spatial and temporal resolution was used. Furthermore, a large-eddy approach for modeling turbulence was chosen. Special care was taken to relate the numerical findings with experimental data. Therefore a geometry was chosen that, in almost full detail, corresponded with an experimental study carried out by Hoekstra et al. (1998a). These authors collected data on the axial and tangential velocity at many points in the cyclone by means of LDA. Furthermore, they were able to visualize vortex-core precession, and extract quantitative data from these visualizations.

The simulations were very well able to qualitatively, and to a large extent also quantitatively, represent the flow system. Vortex-core precession was indeed found to happen with a frequency that was very close to the experimental value (the simulated Strouhal number was within 10% of the experiment). Also the amplitude of the precessing motion matched the experimental data.

The stabilizing effect of the swirling motion on the turbulence was apparent. In the forced vortex region, the flow structures as observed in a horizontal plane were of a markedly different (almost laminar) nature compared to the free vortex region, which was highly turbulent. Speculatively due to the isotropy of the subgrid-scale model, this damping effect caused deviations with experimental data in the average velocity profiles in the core region, albeit that the (still) limited spatial resolution also might have played a role here. The average flow profiles outside the vortex core region were in good agreement with the experimental data.

In subsequent work, solid particles will be released in the flow system in order to simulate its separation capacity. It was demonstrated that the resolution of the flow field was sufficiently high to calculate the trajectories of solid particles typically larger than 10 μm without additional modeling. In the case of smaller particles, the influence of the subgrid-scale motion on the solid particles has to be taken into account. Two-way coupling in an Euler-Lagrange framework appeared feasible, albeit against high computational cost.

It has to be kept in mind, however, that the present simulation was at a moderately valued Reynolds number ($Re =$ 14,000). The step to higher, industrial Reynolds numbers is not straightforward, as the resolution of the boundary layers will become troublesome with the present numerical scheme, based on a uniformly spaced cubic mesh (that is, without the possibility of local grid refinement). There are, however, promising developments in the field of lattice-Boltzmann modeling that allow for local grid refinement. For a brief overview on the latter subject, see Chen and Doolen (1998).

Finally, we remark on the role LES could play in industrially oriented CFD. It was demonstrated in the present article [and also in Derksen and Van den Akker (1998) for the case of a turbulently stirred tank] that complex flow phenomena (here the precessing vortex core) could be resolved very well by our LES-based approach. The high computational intensity compared to RANS simulations make LES less suited for day-to-day CFD applications. The rapid improvements in hardware, as well as in numerics, can change this picture significantly within the short term. The high parallel computational efficiency of the lattice-Boltzmann scheme then certainly is an advantageous feature, as computer hardware developments promote (PC-based) distributed memory computing.

Acknowledgment

The authors thank A. J. Hoekstra for many stimulating discussions on cyclonic flow.

Literature Cited

Bhatnagar, P., E. P. Gross, and M. K. Krook, "A Model for Collision Processes in Gases in Small Amplitude Processes in Charged and Neutral One-Component Systems," *Phys. Rev.*, **94**, 511 (1954).

Boysan, F., W. H. Ayers, and J. Swithenbank, "A Fundamental Mathematical Modelling Approach to Cyclone Design," *Trans. Inst. Chem. Eng.*, **60**, 222 (1982).

Chen, S., and G. D. Doolen, "Lattice Boltzmann Method for Fluid Flows," *Annu. Rev. Fluid Mech.*, **30**, 329 (1998).

Derksen, J. J., J. L. Kooman and H. E. A. Van den Akker, "A Parallel DNS Implementation for Confined Swirling Flow," *Euromsim HPCN Challenges in Telecomp and Telecom*, Delft, The Netherlands (1996).

Derksen, J. J., and H. E. A. Van den Akker, "Large Eddy Simulations on the Flow Driven by a Rushton Turbine," *AIChE J.*, **45**, 209 (1999).

Dyakowski, T., and R. A. Williams, "Modelling Turbulent Flow Within a Small-Diameter Hydrocyclone," *Chem. Eng. Sci.*, **48**, 1143 (1993).

Eggels, J. G. M., and J. A. Somers, "Numerical Simulation of Free Convective Flow Using the Lattice-Boltzmann Scheme," *Int. J. Heat and Fluid Flow*, **16**, 357 (1995).

Eggels, J. G. M., "Direct and Large-Eddy Simulations of Turbulent Fluid Flow Using the Lattice-Boltzmann Scheme," *Int. J. Heat Fluid Flow*, **17**, 307 (1996).

Elgobashi, S., "On Predicting Particle-Laden Turbulent Flows," *Appl. Sci. Res.*, **52**, 309 (1994).

Escudier, M. P., J. Bornstein, and N. Zehnder, "Observations and LDA Measurements of Confined Turbulent Vortex Flow," *J. Fluid Mech.*, **98**, 49 (1980).

Fokke, M. G. D., T. L. Liem, J. J. Derksen, and H. E. A. Van den Akker, "LDA and LIF Experiments on the Quasi-Periodic and Complex Flow in a Cyclone," *Int. Symp. Applications of Laser Techniques to Fluid Mechanics*, Lisbon (1994).

Frisch, U., B. Hasslacher, and Y. Pomeau, "Lattice-Gas Automata for the Navier-Stokes Equation," *Phys. Rev. Lett.*, **56**(14), 1505 (1986).

Griffiths, A. J., P. A. Yazdabadi, and N. Syred, "Alternative Eddy Shedding Set Up by the Nonaxisymmetric Recirculation Zone at the Exhaust of a Cyclone Dust Separator," *J. Fluids Eng.*, **120**, 193 (1998).

Gupta, A. K., D. G. Lilly, and N. Syred, *Swirl Flows*, Abacus Press, Tunbridge Wells, U.K. (1984).

Hinze, J. O., *Turbulence*, McGraw-Hill, New York (1959).

Hoekstra, A. J., A. T. Israël, J. J. Derksen, and H. E. A. Van den Akker, "The Application of Laser Diagnostics to Cyclonic Flow with Vortex Precession," *Int. Symp. Applications of Laser Techniques to Fluid Mechanics*, Lisbon (1998a).

Hoekstra, A. J., E. Van Vliet, J. J. Derksen, and H. E. A. Van den Akker, ''Vortex Core Precession in Gas Cyclones,'' *Advances in Turbulence*, Vol. VII, Kluwer Dordrecht, The Netherlands, (1998b).
Hoekstra, A. J., J. J. Derksen, and H. E. A. Van den Akker, ''An Experimental and Numerical Study of Turbulent Swirling Flow in Gas Cyclones,'' *Chem. Eng. Sci.*, **54**, 2055 (1999).
Hoffman, A. C., A. van Santen, R. W. K. Allen, and R. Clift, ''Effects of Geometry and Solid Loading on the Performance of Gas Cyclones,'' *Powder Technol.*, **70**, 83 (1992).
Kim, J., P. Moin, and R. Moser, ''Turbulence Statistics in Fully Developed Channel Flow at Low Reynolds Number,'' *J. Fluid Mech.*, **177**, 133 (1987).
Piomelli, U., P. Moin, and J. H. Ferziger, ''Model Consistency in Large Eddy Simulation of Turbulent Channel Flows,'' *Phys. Fluids*, **31**, 1884 (1988).
Qian, Y. H., D. D'Humiéres, and P. Lallemand, ''Lattive-BGK Models for the Navier-Stokes Equation,'' *Europhys. Lett.*, **17**, 479 (1992).
Smagorinsky, J., ''General Circulation Experiments with the Primitive Equations: 1. The Basic Experiment,'' *Mon. Weather Rev.*, **91**, 99 (1963).
Somers, J. A., ''Direct Simulation of Fluid Flow with Cellular Automata and the Lattice-Boltzmann Equation,'' *Appl. Sci. Res.*, **51**, 127 (1993).
Stairmand, C. J., ''The Design and Performance of Cyclone Separators,'' *Trans. Inst. Chem. Eng.*, **29**, 356 (1951).
Van Driest, E. R., ''On Turbulent Flow Near a Wall,'' *J. Aero. Sci.*, **23**, 1007 (1956).
Wunenburger, R., B. Andreotti, and P. Petitjeans, ''Influence of Precession on Velocity Measurements in a Strong Laboratory Vortex,'' *Exp. Fluids*, **27**, 181 (1999).
Yazdabadi, P. A., A. J. Griffiths, and N. Syred, ''Characterization of the PVC Phenomena in the Exhaust of a Cyclone Dust Separator,'' *Exp. Fluids*, **17**, 84 (1994).
Zhou, L. X., and S. L. Soo, ''Gas-Solids Flow and Collection of Solids in a Cyclone Separator,'' *Powder Technol.*, **63**, 45 (1990).

Manuscript received Aug. 31, 1999, and revision received Jan. 3, 2000.